Optics Letters

Investigating the dynamic behavior of thermal distortions of the wavefront in a high-power thin-disk laser using the moiré technique

Mohammad Hossein Daemi[1] and Saifollah Rasouli[1,2,*]

[1]Department of Physics, Institute for Advanced Studies in Basic Sciences, Zanjan 45137-66731, Iran
[2]Optics Research Center, Institute for Advanced Studies in Basic Sciences, Zanjan 45137-66731, Iran
*Corresponding author: rasouli@iasbs.ac.ir

Received 12 May 2020; revised 13 July 2020; accepted 14 July 2020; posted 14 July 2020 (Doc. ID 396830); published 11 August 2020

We measure wavefront (WF) distortions in a high-power thin-disk laser induced simultaneously by the gas-lens/wedge and disk front-surface deformation using a two-channel moiré-based WF sensor. Thermal lensing and tilting effects are characterized versus time, their pressure-dependent fluctuations are quantified, and finally the corresponding pure disk front-surface effects are estimated for zero pressure. A divergent probe beam with a WF mean curvature similar to the curvature of the disk is reflected off the disk front surface. The temporal evolution of the WF at laser start-up is characterized using the WF sensor. A camera records both temporal evolution of the moiré fringe patterns and the intensity profile of the laser beam to have simultaneously both phase and intensity profiles of the laser beam. Successive WF data quantify the temporal evolutions of the dioptric power and induced wedges in two directions and their fluctuations during laser operation. We investigate the effect of air pressure on the produced gas-lens/wedge. The method is not sensitive to translational vibrations and is very low cost with adjustable sensitivity.

https://doi.org/10.1364/OL.396830

Thermal lensing of the gain medium of solid-state lasers usually is an unwanted but important effect that should be taken into account in the laser resonator designing. This effect finds more attention in high-power lasers, because of the higher dioptric power of the resulted thermal lens. Although, compared to the traditional rod-type lasers, in a high-power thin-disk laser (TDL) the dioptric power variation range is considerably low thanks to the nearly unidirectional heat flow from the gain medium along the resonator axis, the distribution of the optical path difference (OPD) is important for producing high-quality beams. In a TDL, the thermal effects of the bulk of the gain medium have three major contributions: the bending of the disk, the temperature-dependent refractive index of the medium, and the non-uniform thermal expansion of the medium due to a finite pump spot diameter on the disk [1]. The laser beam experiences these effects simultaneously and in order to design a resonator with a good beam quality, one should measure the resulted OPD, precisely [2].

On the other hand, the resonator generally is flooded with a gas and usually with air. In kW-class TDLs, the temperature increase of the disk surface can be in the order of some tens of Celsius. In such circumstances, the surface of the disk will warm the ambient gas and then produce a phase object in front of the disk because of the temperature-dependence of the refractive index of the gas. The temperature profile of the gas imitates the temperature profile of the disk's surface in the regions near the surface, which fades out in a few millimeters [3,4]. On the other hand, in the presence of gravity, there will be another component for the phase object. This component is a gas-wedge that is due to the upward motion of warm gas that will produce an optical wedge with the thicker side down (in general for gases, $dn/dT < 0$). The optical power of this wedge depends on the pumping power [3,4] and gas density. This effect leads to a resonator misalignment and therefore causes power and/or pointing drift of the laser output beam [5]. This phase object can also couple the degenerate modes of the resonator [6,7].

The worse thing is that the phase object in general has a dynamic nature that causes dynamic distortions of the beam phase-distribution. This can deteriorate the beam's pointing stability, or disturb the modal content in a multimode beam [6].

There are various methods for gain medium OPD measurement, including characterization of the WF of an expanded probe beam passing through the medium or investigation of the borders of the resonator stability regions as a probe-less method [8]. The probe-beam-based methods include interfering of the probe beam with a non-distorted copy of it [2,9], the use of a Shack-Harman sensor [10], and (in the case of positive and strong enough dioptric power) one can find the dioptric power by finding the focus point of the probe beam after passing the medium [3].

Here we investigate the simultaneous behavior of OPD of the phase object and disk front-surface in a kW-class TDL. For this purpose, we developed (both in arrangement and fringe analysis) a moiré-based WF sensor. The moiré-based WF sensor has previously been used in atmospheric turbulence studies [11,12] and in Airy and vortex beams characterization [13,14]. A probe beam is reflected off from the disk surface, and hence

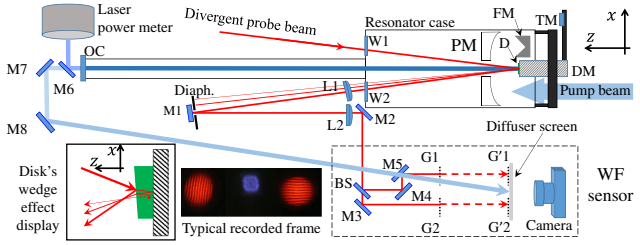

Fig. 1. Schematic view of the experimental setup (drawing is not to scale; see also Visualization 1).

contains the OPD information of the air medium simultaneously with the topography of the disk surface. To investigate the effect of the air pressure on the specifications of the mentioned phase object, we manufactured a high power TDL with a resonator enclosure that can be evacuated. The gain medium of the laser is a thin disk-shaped Yb:YAG crystal with 0.2 mm of thickness and of 20 mm diameter glued on a stiff substrate which is pumped with a fiber-coupled 938 nm diode-laser up to 3 kW using a 16-pass configuration [15]. The nearly flat-top spot size of the pump on the disk surface is about 12 mm. The temperature of the disk's surface at 3 kW pump level is 101°C, which is supported by a cooling system of a 15°C water flow impinging the backside of the substrate. The measured temperature is independent of the air pressure inside the resonator enclosure. A linear resonator with the length of about 3 m is used to produce a multimode laser beam with the beam quality factor of $M^2 \sim 10$ using an output coupler mirror with a 97% reflectivity at 1030 nm and convex radius of curvature (ROC) of 4.5 m. The laser output power is 1.15 kW, and the intra-cavity circulating power is about 38 kW.

Figure 1 shows a schematic view of the laser pump-module, its resonator, and the arrangement to measure 2D profiles of the phase object consisting of a two-channel moiré-based WF sensor, in which each channel measures tip or tilt component of the angle of arrival, which is known as the "moiré-based WF sensor" [12].

The linear resonator is composed of the disk (**D**) attached to the disk-mounting module (**DM**), and an output coupler (**OC**) mirror. The gain medium is pumped in a 16-pass pump-module. The setup is composed of a parabolic mirror (**PM**) and folding mirrors (**FM**).

The probe beam is a divergent 633 nm beam of a He-Ne laser, which entirely covers the disk surface. This wavelength has an appreciable reflectance from the front-surface of the disk (although it is anti-reflective-coated for relevant IR wavelengths). Using the dependencies of the air refractive index on the wavelength, air pressure, and temperature [16], the error induced on dn/dT due to using a 633 nm probe instead of 1030 nm is about 1% or less. We tune the divergence angle of the probe beam so that the beam reflected from the concave disk be nearly flat. Five flat mirrors **M1**–**M5** steer the probe beam toward the gratings. The used disk has a small wedge angle between its back and front surfaces, therefore using a diaphragm (**Diaph.**) we can easily select the beam reflected off the front surface of the disk, to cancel the OPD changes inside the medium (see lower-left inset of Fig. 1). The probe beam enters the resonator enclosure and exits from it through the optical windows **W1** and **W2**, respectively. The existence of such windows enables us to evacuate the enclosure. Considering the positions of the W1 and W2 windows, the angle of incidence is ∼60 mrad. To monitor the thermo-mechanical reaction of the laser structure, a test mirror (**TM**) is attached to DM outside of the enclosure case, to detect and potentially cancel the occurred mechanical drifts in the orientation of the disk. **L1** and **L2** (both with a focal length $f = 100$ cm and with suitable distances from other elements) are lenses of a 4-f imaging system. In this scheme, the gain medium and the primary gratings of the WFS are located at the conjugate planes of the imaging system. The use of a 4-f imaging system fixes the probe beams' sizes and locations on the WF sensor during the experiment.

The WF sensor (shown in a dashed box in Fig. 1) has a beam-splitter **BS** for generating two copies of the beam. **G1** and **G2** are the primary gratings used in each channel. **G'1** and **G'2** are the secondary gratings. All of the gratings have the same period $q = 0.1$ mm. The overall orientation of the lines of the gratings is vertical for one of the channels, and horizontal for the other one. The distance between the gratings in each channel is $Z_T = 225$ mm, which is a half-multiple of the Talbot-distance. At the Talbot-distance, the diffraction of a beam from a linear grating will produce an intensity grating similar to the diffracting grating. The overlap of this intensity grating with the slightly rotated physical grating will produce a rotational moiré fringe pattern whose period depends on the angle of rotation via the relation $q_m \sim q/\theta$ (θ measured as radian). The moiré patterns of the channels are formed on a diffuser screen beneath the secondary gratings. We tune in-plane rotation angles of the secondary gratings to have about 15 fringes on each of the moiré patterns.

Any deviation of the WF will deform/translate the Talbot self-images, which in turn will deform/translate the moiré fringes pattern with a magnification factor q_m/q (see Visualization 1). As the method has high sensitivity, it can visually be used to show the tip/tilt angles' variations even for the fine-alignment of the disk.

The output beam from OC is steered onto a power meter by mirror **M6**. To record the laser beam profile simultaneously with the moiré patterns, a small power-fraction of the beam from the leakage of the mirror M6 is steered by mirrors **M7** and **M8** onto the same diffuser screen used to localize the moiré patterns. A camera records the temporal evolution of the moiré patterns and the laser beam profile, simultaneously. A typical recorded frame by the camera is shown in the lower middle of Fig. 1.

By applying the pumping power, the fringes do in-plane rotation by an angle α_F (see Fig. 2). It can be easily shown that the value of α_F, determines the dioptric power change of the gain medium in the respective plane via the relation $D_{\text{th}} = (q/q_m Z_T) \tan \alpha_F$.

In this work, we extract the local angular deviations of the WF by analyzing the spatial phase of the moiré fringe pattern. If the patterns' lines are aligned along vertical or horizontal directions, their spatial phase along the respective directions are constant (i.e. with zero slope). However, by rotation of the fringe pattern the spatial phase will get a slope value along the initial direction of fringes. The magnitude of the slope depends on the fringe rotation value α_F, and consequently on the ROC change of the WF. Each fringe pattern has also a large slope value perpendicular to the fringe lines because of the high-frequency carrier wave. Considering the first frame as the reference, subtraction of it from the successive frames will cancel this high-value phase gradient, and the temporal variation of the

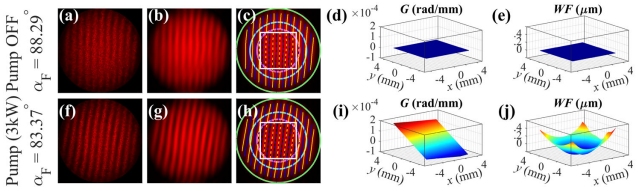

Fig. 2. (a) and (f) Typical fringes recorded before and after, respectively, turning on the laser with 3 kW of pump power. (b) and (g) The corresponding high-frequency filtered patterns. (c) and (h) Fringe traces. The values of fringes angle α_F are for traces inside the magenta-colored circles of ∼9 mm diameter. The green circles show the ∼17 mm of the illuminated region of the disk with the probe beam. The cyan-colored circles show the pump spot of ∼12 mm. The WF profile can be determined by the fringes rotation or by the fringe phase distribution. (d) and (i) The fitted planes to the local slopes of the WF, respectively, before and after applying the pump power. The white-colored squares on (c) and (h) show the calculation. (e) The reference WF that is plane and (j) is a curved WF after applying the pump power (see Visualization 2).

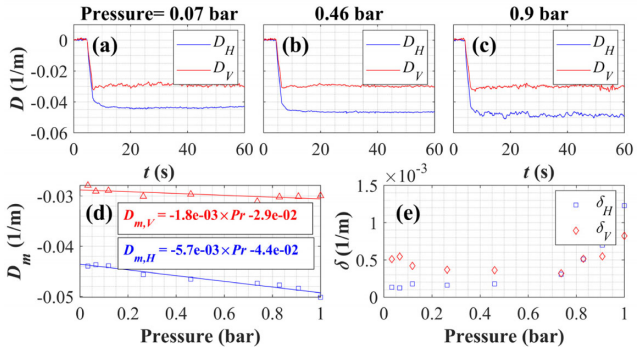

Fig. 3. (a)–(c) Temporal evolution of the measured dioptric power for horizontal (D_H) and vertical (D_V) directions for different values of air pressure during a one-minute period. (d) and (e) Mean dioptric power D_m and standard deviation δ of the fluctuations of D after pump reached its set value, respectively.

phase can be determined. For the case of net tilt of the WF, the fringes move along their normal direction. This movement of the pattern changes the mean value of the spatial phase over the fringe pattern without changing its slope.

Here the Fourier method is very suitable for fringes evolution analysis. For each recorded frame, we calculate the spatial distribution of the phase of the fringe patterns as below:

- After noise filtering of the patterns, do a 2D discrete Fourier transform on each recorded pattern.
- Isolate the positive frequency component of the resulted complex pattern in the spatial frequency domain.
- Do inverse 2D Fourier transform on the positive frequency distribution. The result is a 2D data of complex numbers.
- For each pattern, calculate the phase distribution Φ_{V_W} and Φ_{H_W}.
- Unwrap Φ_{V_W} and Φ_{H_W} and subtract the phase of the reference frame to achieve the continuous phase profiles Φ_V and Φ_H for the selected frame. The phase profiles are representatives of the WF gradient distribution via the relation $G_{V,H} = (q/2\pi Z_T)\Phi_{V,H}$.
- Fit to $G_{V,H}$ a plane of the form $\mathcal{G}_{V,H} = a_{V,H} + b_{V,H}x + c_{V,H}y$.
- ROCs of the WF in vertical and horizontal directions are $1/c_V$ and $1/b_H$ respectively. Because the linear dependence of the WF gradient on position is equivalent to quadratic dependence of the WF of W. Considering formula $W = x^2/2R$ for a paraboloid with R as the ROC, we have $R_H = 1/b_H$. Therefore, the linear coefficients of $\mathcal{G}$ show dioptric powers of the induced lens in the respective directions. The overall tilts are a_V and a_H for the respective directions.
- One can go further to reconstruct the WF W and calculate its specifications. Fitting a 2D polynomial of $W_S = ax^2 + by^2 + cxy + dx + ey + f$ to W, the ROCs of the WF in two directions are $R_x = 1/2a$ and $R_y = 1/2b$, and its tilts are d and e.

We multiplied or divided the calculated diopter values by cos(60 mrad) for vertical and horizontal planes, respectively, in order to compensate for the effect of non-normal incidence.

We performed some experiments with different values of (absolute) air pressure. A rotary vane vacuum pump is employed for this purpose. The temporal behavior of the dioptric power and overall tilts of the WF, simultaneously with the laser beam intensity profile are measured for different values of the air pressure inside of the resonator. In the case of low pressures (in the range of mbar), some points on the optical elements inside the resonator start to glow. To avoid probable damage, the experiments are limited to pressure values higher than 0.03 bar. The pump power reaches its set-value in 2 s. The room temperature and relative humidity were 20°C and 50%, respectively. The temperature of the disk surface is measured using a thermal camera through a ZnSe window. In each experiment, using a camera with a capturing rate 30 fps, the evolution of the moiré patterns, and the laser beam profile are captured for a duration of approximately one minute, started a few seconds before the pump powers on. Two fixed boxes are selected on the successive frames of the recorded movie, each containing an area of 8×8 mm^2 from a pattern. Spatial phase distributions are extracted using the described Fourier algorithm. Considering the first frame as the reference, the temporal evolution of the phase profile, subsequently the relative WF dioptric power and tilt were extracted for the vertical and horizontal directions. At the same time, the simultaneous beam intensity profile relates to the evolution of the phase pattern.

Figure 3 shows the measured dioptric power evolution of the disk front-surface and air at different air pressure values. The figure also shows the mean dioptric power changes $D_{m,H}$ and $D_{m,V}$ for different pressure values. Considering that the initial ROC is about 4 m with a negligible astigmatism (measured using a collimated probe beam), different values for $D_{m,H}$ and $D_{m,V}$ represent the astigmatism of the induced lens. The mean values show approximately a linear dependence on the pressure with different slope values. This implies that the astigmatism of the dioptric power depends linearly on pressure. Extrapolation to zero pressure determines the disk's front-surface dioptric power and its astigmatism. The excess diopter may be attributed to the gas-lens. The standard deviation δ for dioptric power is shown in Fig. 3(e) as a measure to quantify the dioptric power fluctuations. δ_H has a nonlinearly increasing dependence on the air pressure. However, δ_V does not have such a monotonic behavior. Figure 3(e) indicates that even at the pressures close

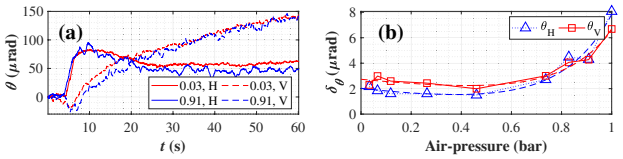

Fig. 4. (a) Measured tilts of the probe beam in the horizontal and vertical directions for two different values of the air pressure. (b) The standard deviation of the fluctuations as the pressure of the resonator case.

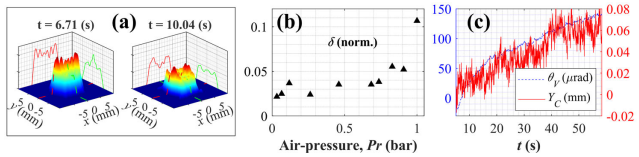

Fig. 5. (a) Beam profiles at two different times for air pressure of 1 bar. (b) Standard deviation of the normalized power at different values of pressure. (c) Simultaneous plot of the phase front vertical tilt of the probe beam and the laser beam vertical position, Visualization 3.

to zero still there are dioptric power fluctuations that can be considered as the pure effect of surface fluctuations.

Temporal behavior of the tilt angles are depicted in Fig. 4. Beside a slowly varying drift, the tilt angles have instantaneous fast fluctuations. The slowly varying tilts are related to the thermo-mechanical reaction of the structure of the instrument. The horizontal tilt has a large 70 micro-radian rise at the beginning, which is damped slightly afterward. As the disk has a wedge-like structure which is bonded firmly on a stiff substrate, under thermal load the wedge angle changes. Since we aligned the disk-wedge direction horizontally, under thermal load the observed fast rise in the horizontal direction is related to the wedge angle of the disk. Based on Fig. 4, the thermo-mechanical reactions of the resonator case and disk mount (Fig. 1) are such that they try to compensate the excessed wedge effect induced on the disk in the horizontal direction by thermal loading. For the vertical tilt, the gas wedge that tries to tilt the probe beam downward causes an initial small drop, but the reaction of the structure opposes it, which is able to reverse the tilt sign. To evaluate the net dynamic behavior of the gas-wedge, we subtracted the slow variations from the calculated data. For both horizontal and vertical tilts, we fitted a rational function $F(t) = \sum_{i=0}^{4}(a_i t^i)/(t+b)$ to the data. There is a good agreement between the fitted function and the slow drift of the experimental data. We used the standard deviation δ of the residuals as a measure to quantify the magnitude of the fluctuations. These fluctuations have two major sources: fluctuations of the gas-wedge dioptric power, and angular vibrations of the disk due to the environmental perturbations like the water flow through the disk module. Using a rotation-sensitive laser-Doppler vibrometry method [17], the order of amplitude of the angular vibrations was measured and determined few micro-radians. Contributions of these parameters are not separated, although one can expect that for lower pressure values the contribution of the gas-lens is negligible. To quantify the laser beam, we extract some parameters of the produced beam by analyzing the beam profile in successive frames [Fig. 5(a)]. We normalize the intensity integral as a measure of the instantaneous power. The average power is calibrated to the power measure by a laser power meter. Beam power fluctuations for different values of the air pressure is shown in Fig. 5(b). By comparing Fig. 4 and Figs. 5(b) and 5(c), it is evident that the magnitude of the fluctuations of the phase front tilt with the laser power, and also the phase front tilt with the beam vertical pointing are well correlated, see Visualization 3.

In conclusion, we developed an experimental low-cost method to evaluate temporal evolution of dioptric power and tilt angles of the front-surface in a high-power TDL. A Fourier analysis was used to derive the WF information from the moiré-based measurements. Our measurements disclosed the probable vibrational and thermo-mechanical imperfections that might occur in the design and manufacturing of the laser head, which must be considered for development of a reliable laser.

Acknowledgment. M. H. D. thanks the INLC for their support.

Disclosures. The authors declare no conflicts of interest.

See Supplement 1 for supporting content.

REFERENCES

1. B. Weichelt, D. Blazquez-Sanchez, A. Austerschulte, A. Voss, and T. Graf, Proc. SPIE **7721**, 77210M (2010).
2. J. Perchermeier and U. Wittrock, Opt. Lett. **38**, 2422 (2013).
3. A. Diebold, F. Saltarelli, I. J. Graumann, C. J. Saraceno, C. R. Phillips, and U. Keller, Opt. Express **26**, 12648 (2018).
4. T. Dietrich, C. Röcker, T. Graf, and M. Abdou Ahmed, Appl. Phys. B **126**, 47 (2020).
5. T. Dietrich, S. Piehler, C. Rocker, M. Rumpel, M. Abdou Ahmed, and T. Graf, Opt. Lett. **42**, 3263 (2017).
6. R. Paschotta, Opt. Express **14**, 6069 (2006).
7. Q. Zhang, B. Ozygus, and H. Weber, Eur. Phys. J. Appl. Phys. **6**, 293 (1999).
8. M. Shayganmanesh, M. H. Daemi, S. Radmard, and S. Kazemi, Opt. Laser Technol. **44**, 2292 (2012).
9. M. R. Jafarfard, M. H. Daemi, and S. Kazemi, J. Opt. Soc. Am. B **36**, 2884 (2019).
10. J. Mende, E. Schmid, J. Speiser, G. Spindler, and A. Giesen, Proc. SPIE **7193**, 71931V (2009).
11. M. Dashti and S. Rasouli, J. Opt. **14**, 095704 (2012).
12. S. Rasouli, M. Dashti, and A. N. Ramaprakash, Opt. Express **18**, 23906 (2010).
13. M. Yeganeh, S. Rasouli, M. Dashti, S. Slussarenko, E. Santamato, and E. Karimi, Opt. Lett. **38**, 887 (2013).
14. D. Abdollahpour, M. Lotfollahi, M. Yeganeh, and S. Rasouli, J. Opt. **21**, 085602 (2019).
15. S. Seyedzamani and E. Eslami, Opt. Eng. **56**, 085106 (2017).
16. P. E. Ciddor, Appl. Opt. **35**, 1566 (1996).
17. S. Rasouli and M. H. Daemi, Opt. Express **28**, 8658 (2020).